Development of a High-Speed Three-Dimensional Flow Visualization Technique

Brian S. Thurow* and Kyle P. Lynch†
Auburn University, Auburn, Alabama 36849

A high-speed three-dimensional flow visualization system has been developed and is described. The technique is based on the high-speed scanning and subsequent imaging of a two-dimensional laser sheet through the flowfield. A three-dimensional image is then reconstructed from the stack of two-dimensional slices. The technique achieves high speeds using a home-built megahertz-rate pulse-burst laser system, a galvanometric scanning mirror, and a high-speed intensified charge-coupled-device camera capable of 500,000 frames per second. These components allow for the acquisition of three-dimensional image data with a resolution of 220 × 220 × 68 volumetric elements (voxels) in 136 μs. The speed of the technique is limited by the available camera speed and can be increased substantially using a higher-speed camera. The technique is demonstrated through three-dimensional visualization a turbulent round jet ($Re = 6700$) seeded with small water droplets for light scattering. Three-dimensional flow visualization images display numerous three-dimensional features of the jet, including ring vortices, azimuthal modes and counter-rotating streamwise vortex pairs. Future work will focus on the development of a high-speed three-dimensional laser-induced fluorescence technique.

I. Introduction

TECHNIQUES available for flow diagnostics have witnessed an evolution from intrusive pitot tubes and anemometers to nonintrusive techniques using lasers. In the past, these laser-based methods were limited spatially to one dimension, such as with laser Doppler anemometry, or to two-dimensional techniques, such as schlieren imaging and 2-D particle image velocimetry (PIV). Because of the inherent spatial and temporal limitations of these techniques, many fluid dynamic problems that are unsteady and three-dimensional in nature cannot be analyzed with the detail necessary to understand the underlying physics. In recent years, however, drastic improvements in imaging speed and resolution have occurred due to advances in charge-coupled-device (CCD) camera design and the demonstration of high-energy, high-repetition rate laser sources. These advanced technologies have allowed improved study of many dynamic flow problems occurring at high speeds with flow visualization [1–3], traditional and stereoscopic particle image velocimetry (PIV) [4,5], planar Doppler velocimetry [4,6], planar laser-induced fluorescence (PLIF) [7,8], and other methods. In addition, the magnitude of these advances has made possible entirely new flow diagnostic techniques.

The focus of this work is on the development and demonstration of a high-speed three-dimensional flow visualization system. A number of efforts have been made over the years to develop 3-D flow measurement systems. These include stereographic [9], holographic [10,11], tomographic [12], and laser-sheet-scanning [13–22] methods. In principle, stereographic-, holographic-, and tomographic-based techniques are capable of acquiring instantaneous three-dimensional flow data, but the practical implementation is limited by complex and sensitive optical setups, restricted optical access in flow facilities, limited camera resolution, costs, and various other factors. In addition, these techniques are generally restricted to particle-based measurements and are not as well suited for flow

visualization or 3-D fluorescence measurements. The approach that has received the most attention and is adopted in this effort is laser-sheet-scanning flow visualization. In this technique, a laser beam is formed into a sheet using cylindrical lenses and is scanned through the flowfield using an optical deflector, such as a rotating mirror. As the laser sheet passes through the flowfield, a sequence of images at different planes throughout the flowfield is acquired. A 3-D image can then be reconstructed from the stack of images.

The amount of time it takes to scan the laser sheet through the flowfield and acquire images at each cross section creates inherent limitations in the speed of the flows that can be studied, with most studies limited to very low speed (less than 1 m/s) flows. High-repetition-rate lasers, high-speed cameras, and various optical deflectors have been previously employed to allow the technique to be applied to high-speed flow applications. Long and Yip [14] and Yip et al. [15] used a resonant scanning mirror to deflect the output of a dye laser with a 1.4-μs-duration pulse through the flowfield. During the sweep of this single pulse, 12 images, each with a resolution of 58×120 pixels, were acquired with an electronic framing camera operating at 10 MHz framing rate. Patrie et al. [16] improved upon this technique by using a higher-energy pulsed dye laser (10 J/pulse), a 12-sided polygonal mirror rotating at 500 Hz, and a camera capable of acquiring 20 images at a resolution on the order of 120×90 pixels for each image. Island et al. [18] subsequently used the technique to perform the first nearly instantaneous 3-D flow visualization of a supersonic flow. Hult et al. [21] used a cluster of four double-pulse Nd:YAG lasers, a galvanometric scanning mirror, and an 8-CCD (i.e., eight frames) high-speed camera to obtain a sequence of eight images (576×285 pixels each) in a 15 m/s reacting flowfield over a span of $\sim$88 μs. Their technique used laser-induced incandescence to measure soot volume fractions in a flame. Although not as fast as the previously mentioned techniques, the advantage of their approach was the use of pulsed ($\sim$10-ns-duration) Nd:YAG lasers for which the output can be more efficiently converted to second, third, and fourth harmonics and is compatible with a large number of existing planar techniques. In all cases, the speed, resolution, and maximum number of frames of the high-speed camera as well as the capabilities and flexibility of the laser system were limiting factors.

Since these earlier works, a number of advances have been made in laser and camera technology that allow for a refreshed look at the concept of high-speed scanning for 3-D imaging purposes. In particular, this paper details the development of a new flow visualization system that uses the unique capabilities of a recently developed

*Associate Professor, Advanced Laser Diagnostics Laboratory Department of Aerospace Engineering. Member AIAA.

†Graduate Research Assistant, Advanced Laser Diagnostics Laboratory Department of Aerospace Engineering. Student Member AIAA.

megahertz-rate pulse-burst laser system. The 3-D flow visualization system consists of a pulse-burst laser, a galvanometric scanning mirror, and a high-speed camera. These components and their function within the system are described here. In addition, the technique is demonstrated by visualizing the flow of a turbulent jet, which reveals the potential for this technique to explore 3-D phenomena in a wide variety of turbulent flows.

II. System Overview

Figure 1 presents a schematic view of the 3-D flow visualization system. A burst of high-energy laser pulses is first passed through a long-focal-length spherical lens and then reflected from the surface of a rotating mirror. The deflected pulses then pass through a cylindrical lens, forming a thin laser sheet. A high-speed camera is used to capture images of each successive laser pulse as it illuminates a 2-D slice of the flowfield. The resulting stack of 2-D images is then used to reconstruct and display a 3-D image of the flow. The high-speed characteristics of the system are determined by the speed of the laser, mirror, and camera. In this section, we describe each of these components, placing particular emphasis on their speed and how they function within the 3-D flow visualization system.

A. Megahertz-Rate Pulse-Burst Laser System

The pulse-burst laser system was developed at Auburn University and is a third-generation design. It is based on similar systems described by Lempert et al. [23], Wu et al. [1], and Thurow et al. [24]. The detailed design and performance of the system used in this work is reported in Thurow et al. [25], with a brief description provided here. The fundamental concept of the laser system is to generate and amplify a train of short-duration laser pulses to high energies. The initial laser output is provided by a 100 mW continuous-wave diode-pumped Nd:YAG laser, with output at 1064 nm. The output beam is tightly focused through an acousto-optic modulator (AOM), which uses the acousto-optic effect to deflect the incident laser beam. Short-duration pulses with high extinction ratio are contained in the deflected beam path and formed by cycling the AOM between its off and on states. The AOM's speed is characterized by a rise/fall time of 10 ns. Thus, pulses as short as 20 ns in duration and at repetition rates as high as 50 MHz can be produced. At this stage, the laser pulses contain on the order of 1 nJ of energy per pulse and must be amplified to be useful for general flow diagnostics. This is accomplished using a power amplifier chain. The chain consists of three double-pass flashlamp pumped Nd:YAG rod laser amplifiers with diameters of 4, 5, and 6.3 mm, respectively. Each stage is isolated from the others using Faraday isolators, which helps to minimize parasitic oscillations, amplified spontaneous emission, and self-lasing of the entire system. Energy (30, 30, and 40 J, respectively) to the flashlamps is provided using a custom-built power supply that provides relatively uniform current to the flashlamps over a 0.8 ms period of time and provides an envelope in time over which high-energy pulses can be generated. The overall system gain during this time is approximately 2×10^5 for the experiments reported herein.

Following amplification, the output is frequency-doubled to 532 nm, which provides for more efficient scattering from particles and is better matched with the sensitivity of conventional CCD cameras. Second-harmonic generation is achieved using an $8 \times 8 \times 8$ mm KTP type II nonlinear optical crystal. Conversion efficiencies of up to 37% have been achieved with aggressive focusing and collimation of the beam before entering the crystal; however, to prevent crystal and optics damage, less aggressive focusing using a +1000 mm lens has been used, with a decrease of conversion efficiency to ~10%. For the experiments described herein, each burst consists of 68 laser pulses produced at 500 kHz. Each laser pulse is 250 ns in duration, with approximately 1 mJ of energy per pulse at 532 nm.

It should be noted that the laser is currently being upgraded through the addition of two more amplification stages and a new higher-power flashlamp power supply, which is expected to produce pulse energies in excess of 100 mJ/pulse over a 20-ns-duration laser pulse. In addition, a fourth-harmonic generator is being constructed to enable conversion to 266 nm for fluorescence measurements.

B. Ultra-High-Speed Camera

A DRS Hadland Ultra68 high-speed camera is used to capture images of the laser sheet as light is scattered by particles present in the measurement volume. The camera is capable of capturing 68 separate 220×220 pixel resolution images at up to 500,000 frames per second with individual exposure times as short as 10 ns. To achieve these high speeds and high number of frames, the Ultra68 combines several approaches commonly used to acquire images at very high speeds. First, light entering the camera is divided using a four-way beamsplitter, creating four separate optical paths. Four nearly identical images are thus formed on the surface of a four-quadrant image intensifier. Each quadrant of the intensifier is controlled independently, allowing for high frame rates to be achieved by firing each quadrant in succession. This architecture allows for four high-speed images to be acquired at rates as high as 100 MHz, although this speed has not been verified with this particular camera. A $2k \times 2k$ CCD sensor is located behind the intensifier to record the images formed in the four quadrants. As will be discussed, this architecture introduces minor dissimilarities between the four images, due to slight differences in the optical path, intensifier gain, and gain uniformity which must be corrected for in the postprocessing steps.
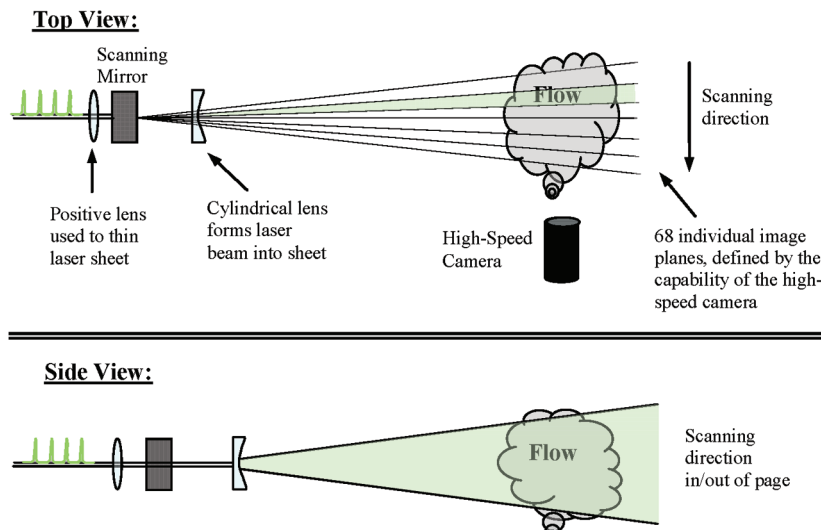

Top View:

Scanning Mirror

Positive lens used to thin laser sheet

Cylindrical lens forms laser beam into sheet

High-Speed Camera

Flow

Scanning direction

68 individual image planes, defined by the capability of the high-speed camera

Side View:

Flow

Scanning direction in/out of page

Fig. 1 Schematic of laser-sheet-scanning technique for 3-D flow visualization.

To achieve even higher frame-storage capabilities, the CCD surface is covered by a specialized opaque mask that blocks light from 16 out of every 17 pixels. Thus, only one pixel out of 17 is exposed to light. The remaining pixels are used to store charge produced at the exposed pixel by rapidly shifting the charge from the exposed pixel to one of the pixels behind the mask, which can be thought of as on-chip memory modules. In this fashion, 17 sequential images can be stored by the CCD at up to 125,000 frames per second. While this results in a relatively low fill factor for the sensor (less than 3%), the coupling with the segmented intensifier allows for the acquisition of a sequence of 68 images, each with a resolution of 220×220 pixels, at frame rates as high as 500,000 frames per second. Thus, a sequence of 68 images takes 136 μs to acquire. It should be noted that a number of alternative methods (i.e., multiple sensors, specialized CCD chips, etc.) exist with respect to high-speed cameras that may allow for higher-resolution images, higher frame rates, and a greater number of frames. As will be seen, the camera available for this study is currently the limiting factor to the speed and resolution of this technique, but suitable to demonstrate the general capabilities of the technique.

C. High-Speed Laser Scanner

A number of devices were considered for high-speed scanning of the laser sheet, including rotating mirrors, acousto-optic deflectors, and electro-optic deflectors. To characterize the performance of each of these devices, the number of resolvable spots, slew rate, and random access time were compared, as well as other factors.

The number of resolvable spots is defined as the number of distinct angular positions that can be attained during a scan. This is given as a ratio of the total scan angle to the divergence of the laser beam:

$$N = \frac{\Delta\alpha}{\Delta\phi} \tag{1}$$

where $\Delta\alpha$ is the total deflection angle of the device, and $\Delta\phi$ is the angular divergence of the laser beam. The full angular divergence of a Gaussian laser beam is given by

$$\Delta\phi = \frac{4\lambda}{\pi D} \tag{2}$$

where λ is the wavelength of light, and D is the beam diameter [26]. Note that for a larger incoming beam size (greater D), the angular divergence is reduced and the number of resolvable spots increases. This parameter defines the number of unique image planes that can be accessed in a single scan.

The slew rate denotes the number of resolvable spots accessed per unit time for a single direction sweep and is thus a measure of the angular velocity of the scanning system. The random access time is the time taken for the deflector to go from one random deflection angle to another. A distinction is made between random access time and slew rate, which can vary widely, depending upon the scan device. For the laser-sheet-scanning method described here, the slew rate is the most important parameter, as it determines the time it takes to complete a full sweep.

Electro-optic deflectors provide the highest potential speed, but require high-speed, high-voltage power supplies and small beam sizes to achieve the number of resolvable spots (68) necessary for this technique. This type of deflector is not available commercially and would have to be custom-built. Alternatively, acousto-optic deflectors (AODs) are available commercially with a large number of resolvable spots and short random access time. One such device was tested and found suitable for the current application. The AOD (manufactured by Brimrose) was constructed of fused silica with a 6×1 mm aperture with the acoustic direction along the major axis. The speed of sound within the AO medium is 5960 m/s, which corresponds to a ~1 μs random access time for a 6 mm aperture. Acoustic energy was provided using a 4 W RF driver with frequency tuning from 75 to 125 MHz, yielding a total of 50 resolvable spots. The AOD has a couple of drawbacks, however. First, the deflection efficiency ranged from 30–60% over the scan range, reducing the

amount of light available for imaging. Second, the beam's shape had to be modified from circular to elliptical to fit the aperture of the device and still achieve a large number of resolvable spots, adding additional complexity to the optical arrangement. More details on this AOD can be found in [27]. Still, the AOD was found to be suitable for high-speed scanning and may be the best choice for an application requiring short random access times.

A galvanometric scanning mirror (GSI Lumonics VM500) was found to be optimal for the present application. Similar mirrors have been used in the past for high-speed scanning applications (e.g., [17]) and are relatively economical. A servo (GSI Lumonics MiniSAX) is used to control the mirror's angular position with power provided at ±20 V using a Tenma 72–7245 variable-dc power supply. The mirror's position is set by a variable-command input (maximum 3 V) produced by a National Instruments (NI) PCI-5402 signal generator. The position is output as ±3 V using an internal magnetic encoder connected to the rotating shaft.

The performance of the mirror to a step-command input was tested when the mirror was started at rest and then commanded to move and stop at a new position. Figure 2 presents the deflection angle versus time for the mirror as used in the current experiments. Superimposed on this curve is the command signal to the pulse-burst laser system, indicating the timing of the laser pulses. As can be seen, the laser pulses occur while the mirror is in motion, with the deflection angle varying in an approximately linear fashion over this period of time. A step input (3 deg in Fig. 2) is necessary in order to allow the mirror to accelerate to high speeds and was chosen in this case to produce the observed high-speed motion of the mirror. The maximum slew rate possible with this mirror was measured in excess of $100,000$ deg /s for a step command of approximately 30 deg. This speed was verified by imaging a moving spot produced by a laser beam with the high-speed camera. For a 6 mm Gaussian beam at 532 nm, this corresponds to a peak slew rate of ~18 spots per microsecond with over 2700 resolvable spots available over the entire scan. This slew rate is more than an order of magnitude greater than the camera's framing rate, making it suitable for even higher-speed scans than those demonstrated here. For circumstances in which a lower slew rate is needed, the command input can be varied from a step input to a ramp input, with the slope tailored for the application. In addition to the high slew rate, the mirror demonstrated high repeatability in both deflection speed and positional accuracy from one scan to the next, with no scan-to-scan jitter detected.

A distinct advantage the mirror has over other methods is the high deflection efficiencies that can be achieved using mirrors with high-reflective coatings at specific wavelengths, such as 532 nm. These coatings allow efficiencies of over 98% to be achieved, easing the demands on both the laser system and the camera. Future upgrades include a mirror coated for light at 266 nm, the fourth harmonic of Nd:YAG, to support acetone fluorescence. As such, the system can easily be reconfigured for different experiments. Overall, the mirror proves to be a fast, inexpensive, reliable, and efficient scanning system for 3-D imaging. The main drawback to this type of mirror is a relatively long random access time (compared to acousto-optic
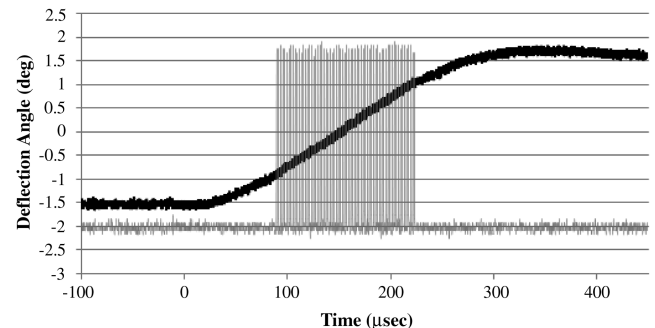

Fig. 2   Timing of linear portion of deflection with laser pulses (0 μs at the time of mirror step-command voltage). Black represents the mirror deflection angle, and gray represents a superimposed graph of 68 laser pulses.

deflectors), which limits its use to linear single-direction sweeps through the flowfield.

D. Component Synchronization

A significant challenge to the laser scanning technique is synchronization of all the components. A schematic of the system synchronization is shown in Fig. 3. The laser amplifier power supply, which operates at an overall repetition rate between 1 and 10 Hz (user-selected) provides the master trigger to which all components in the system are synchronized. This trigger is read into a PC running NI LabVIEW using a NI PCI-6602 counter-timer card. LabVIEW is then used to trigger an external pulse-generator box (Quantum Composers model 9514), which creates the burst of laser pulses with the number of pulses, pulse duration, and burst delay set by the user. This external pulse generator is used due to its higher-resolution time base (100 MHz) compared to the PCI-6602, allowing shorter, higher-quality trigger pulses to be passed to the AOM driver. The burst delay refers to the delay between the firing of the flashlamps and the first laser pulse in the burst. The burst delay is an important parameter in the operation of the laser, as it affects the distribution of energy over the burst of pulses and is chosen to provide as uniform a distribution (less than 10% variation across all pulses) as possible.

Preceding the formation of laser pulses, a step input generated by a NI PCI-5402 signal-generator card is provided to the scanning mirror, commanding it to move. The amplitude of the input determines the maximum speed of rotation and, therefore, the total spread angle of the laser pulses deflected from the mirror. Alternatively, the command input to the mirror can be set as a ramp profile to control the speed of the scan. The laser pulses are produced near the midpoint of the mirror's sweep, where the angular motion is approximately linear. This timing between the mirror's actual motion and the laser pulses is illustrated in Fig. 2, in which the step-command voltage input to the mirror calls for a deflection of ~ 3 deg, and the pulses are deflected approximately 2 deg during the rotation of the mirror. The Ultra68 camera is triggered by LabVIEW approximately 85 ns before the start of the laser pulse train, to account for manufacturer-reported internal delays. Camera software controls the exposure sequence, including the frequency and exposure time.

III. Experimental Facility

The flowfield of a round jet was used as a test bed for the development of the 3-D flow visualization technique described here. This flow possesses a combination of strong axisymmetric features, such as ring vortices, and more complex 3-D features such as the onset of azimuthal instabilities and the transition to turbulent flow in the far field of the jet. The 3-D physics of this flowfield are under further investigation with further details found in Thurow and Lynch [28]. This particular flow was chosen for this study as it was relatively simple and economical to construct, although it should be noted that this technique may be more suited for flowfields that do not possess such strong symmetric features. The jet facility consists of a converging nozzle attached to a settling chamber with honeycomb and a perforated plate used at the nozzle inlet for flow conditioning. Seed particles are generated in a secondary chamber using an ultrasonic mister to create small water droplets that are mixed with the airflow delivered to the nozzle. A fan is used to force the water droplets and air through a 50.8-mm-diam hose and into the settling chamber. The nozzle has a contraction length of 165 mm and an exit diameter D of 30.5 mm. The jet velocity at the exit is measured using a pitot probe to be approximately 3.3 m/s, giving a Reynolds number based on jet diameter of approximately 6700. At this speed, the flow moves less than one pixel over the 136 μs time it takes to complete a scan. Details of the boundary layer at the exit of the nozzle were not measured directly, but the boundary layer is expected to be laminar with a thickness of less than 1 mm.

The laser sheet and camera were set up to image the near field of the jet from $0.85x/D$ to $3.75x/D$, with y representing the transverse axis of each 2-D image and z corresponding to the scan direction. The pulse-burst laser system was set up to output 68 pulses at 500 kHz, which corresponds to the maximum number of frames and maximum speed of the high-speed camera. A Nikon telephoto lens was attached to the camera, adjusted to a focal length of 135 mm, $f2.8$, and focus at 2.7 m. Each 2-D image views an area 89×89 mm with 68 images acquired over a scan length of 64 mm. Thus, the 3-D visualizations capture a volume of $89 \times 89 \times 64$ mm with a resolution of $220 \times 220 \times 68$ volume elements (or voxels).

IV. Image Processing

A number of image processing steps are implemented to improve the quality of the acquired images and to compile theme into a 3-D data cube suitable for display. A single raw 2-D image is shown in Fig. 4. The presence of vortex rings in the shear layer of the jet is clear; however, the image quality is affected by the distribution in light intensity across the laser sheet and the noise/gain characteristics of the intensified camera, which are somewhat unique due to the architecture of the camera discussed earlier. A number of steps are implemented to improve the quality of these images. The order these corrections are performed is as follows: 1) flat-field correction, 2) dark-image subtraction, 3) laser-sheet intensity normalization, 4) spatial correction, and 5) image smoothing.

A. Flat-Field and Dark-Image Corrections

The first image correction performed is a flat-field correction, which corrects for slight differences in sensitivity of individual pixels. These differences can be caused by nonuniform materials in makeup of the CCD and intensifier or slight misalignments in the optical paths leading to the image intensifiers. The Ultra68 camera used here possesses a rather pronounced form of fixed-pattern noise associated with each quadrant of the CCD/intensifier arrangement. The flat-field calibration process consists of placing a plane of uniform intensity in front of the camera lens. This was produced in a dark room using a 60 W frosted light bulb placed 1 m behind a plain white sheet of paper. Software provided by the camera manufacturer takes multiple image sequences and develops a set of intensity coefficients that the pixels of the image sequence are multiplied by to result in an image of constant intensity values. This set of coefficients
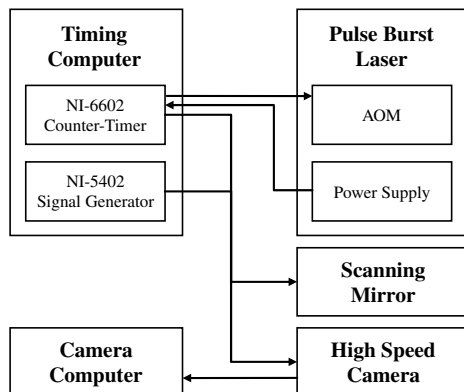

Fig. 3 Relationship of signals between system components.
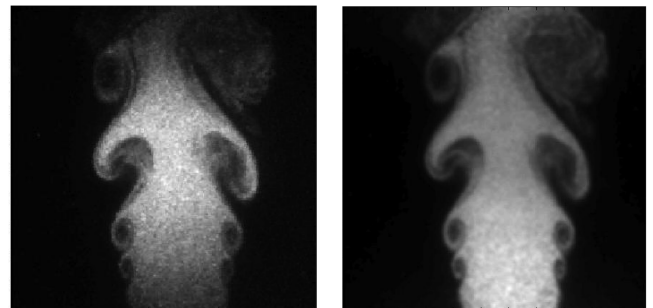

Fig. 4 Images of the center slice (34 out of 68), before (left) and after (right) image processing.

is stored and used by the camera software to correct all subsequent images. To correct for surrounding sources of light visible to the camera, such as the operation of the flashlamp pumped laser amplifiers, a dark image is subtracted from every image captured. This dark image is taken with the same settings as during the experiment, including the firing of the laser flashlamps, but without any laser output from the system.

B. Region and Sheet Intensity Normalization

The roughly Gaussian laser beam produced by the pulse-burst laser system, when passed through a cylindrical lens, becomes a laser sheet with a similar Gaussian intensity profile that varies in the x direction. This profile will accentuate flow features near the center of the sheet and mask features at the edge, as shown in Fig. 4. For the current experiments in which the pulse energy is limited to $\sim$1 mJ/pulse (to be increased in future experiments), this is particularly noticeable. For a better understanding of the effect, a data set of 500 image sequences was taken, from which an average image was calculated. We correct for this variation in laser-sheet intensity using an in situ calibration method. One method of correction would be to treat and correct each 2-D slice of the flow separately; however, we employ a strategy that uses the complete 3-D image data (also referred to as a data cube). Our method begins with the assumption that for a given cross section of the jet (y-z plane), the total number of light-scattering particles should be approximately constant, on average. This is, more or less, a statement of conservation of mass of the number of seed particles. As such, the integrated intensity for a cross-sectional slice (220×68 pixel slice orthogonal to the jet axis) should be constant across different downstream locations. Any fluctuations in the integrated value are thus attributable to streamwise variations in the laser-sheet intensity. This information is used to estimate the average laser-sheet intensity profile, which, in turn, is used to normalize each of the cross-sectional images. Overall, this proved to be a convenient method to correct for obvious variations in the laser-sheet intensity and is suitable for flow visualization purposes. Future efforts in which quantitative information is desired will need to use a more robust calibration method to correct for this effect, as the dynamics of the seed particles (agglomeration, evaporation, condensation, etc.) are not accounted for.

An additional source of intensity variation is due primarily to fluctuations in the power output by the pulse-burst laser system. These slight variations are due to variations in the seed laser output, flashlamp energy, thermal loading of the amplifiers, and various other factors, such as variations of the particle seeding in the jet. For the most part, these variations are found to be more significant from burst to burst, as opposed to between individual pulses in a burst. For statistical analysis using large numbers of image sequences, the image intensity must be normalized to eliminate the effect of pulse train energy fluctuations. To accomplish this, a three-dimensional region of the flowfield in which the intensity is expected to be constant is selected. For these images, a region in the jet core near the nozzle exit is selected. In this region, any changes in intensity are due only to laser energy fluctuations and/or changes in the bulk particle seeding of the jet. Thus, each 3-D image is divided by the average value of the region to accomplish normalization.

C. Spatial Calibration

An additional image processing step that must be considered is calibration of the images in 3-D space. Although not overly important for flow visualization, proper calibration will be crucial for more detailed quantitative measurements such as 3-D laser-induced fluorescence (LIF) or 3-D PIV, in which it is important to know where the signal originated with a high level of precision. The most significant effect is the change in magnification from the front to the back image plane, as illustrated in Fig. 5. In addition, complicating this issue is the four-quadrant architecture of the high-speed camera, which causes a small misalignment between images projected onto each quadrant and appears as a frame-to-frame jitter. Thus, two corrections must be implemented: one to correct for changes in magnification and the other to correct for the frame-to-frame jitter.
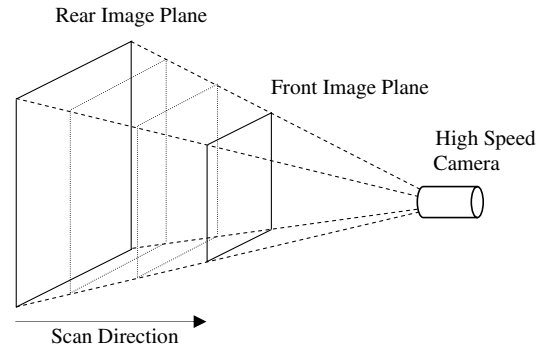

Fig. 5   Geometry of the measurement volume throughout a scan.

To correct both of these problems, a dot-card alignment process was developed and is currently being refined for higher precision. A dot card was constructed out of an aluminum plate by drilling holes in a precise grid pattern. A light source was then placed behind the card to provide clear dot images. The spacing between dots is 12.7 mm, and the dot diameter is 3.18 mm. It has been found that a single dot-card image at the center of the imaging volume is sufficient to correct for the frame-to-frame jitter observed in the images. A single dot card, however, is not sufficient to address the change in magnification of the image through the measurement volume. The most accurate approach would be to acquire a dot-card image for each location of the laser sheet. As the laser sheet scans through 68 different planes, however, this procedure is quite tedious and not practical for many experimental setups. Rather, we take a dot-card image at the rear object plane and a dot-card image at the front plane and interpolate the dot location at intermediate planes. This idea was tested by mounting the dot card on a translation stage and taking dot-card images at seven different locations. The dot locations for each image were found using a center-of-mass dot-finding technique. The dot positions at the front and back planes were then used to estimate the dot location at the intermediate planes using simple linear interpolation. The interpolated dot positions were found to match the physical dot-card image points at the intermediate planes to within subpixel accuracy. The inclusion of additional dot-card images in the calculation may provide even more accurate results. Once the dot locations are determined for each 2-D image, all images in a sequence can be mapped to a common 3-D coordinate system defined by the known dot locations in physical space. This correction, implemented in MATLAB, also accounts for any image distortions that may result from the optical arrangement (e.g., lens, perspective error, etc.). Further work is needed to refine and better quantify the accuracy of this calibration procedure; however, for the purposes of 3-D flow visualization, the present steps are deemed more than sufficient to yield high-quality 3-D views of the flow.

D. Three-Dimensional Image Smoothing

Finally, a 3-D image smoothing step is taken in which a $3 \times 3 \times 3$ averaging filter is applied to the 3-D data cube. This is similar to a conventional low-pass averaging filter used in 2-D images, in which various kernels can be applied to the image for the purposes image smoothing, edge detection, etc. For the data presented here, we use a $3 \times 3 \times 3$ kernel of uniform weights. Application of this filter was found to be important for the display of the 3-D image data, as it helps to meld the separate 2-D images together. This is particularly important with respect to the creation of isosurfaces that use the intensity values found in the image. Figure 4 shows an image before and after all of the corrections were implemented. It can be seen that variations in laser-sheet intensity have been mitigated and the graininess of the image is diminished by the averaging filter. Furthermore, the large-scale structures observed in the image are still clear.

E. Remaining Issues

A long-term goal of this work is to use the general technique outlined here to obtain more quantitative information about the flow, such as an effort currently underway to develop 3-D LIF based on

acetone fluorescence. There are a few outstanding issues that must be dealt with if new techniques are to be successfully developed. These ideas are outlined here with efforts currently underway to address them. Their implementation, however, is not critical to 3-D flow visualization, in which a qualitative understanding of the flowfield is the primary goal.

The most significant of these is an issue known as *ghosting* and commonly associated with imaging at very high speeds. Ghosting is an image artifact in which the signal contained in one frame of the sequence is apparent in other frames of the sequence as well. A preliminary investigation of this problem has been conducted by using a single laser pulse to visualize the flow in a single frame and observing the images produced in subsequent frames in which no signal should be present. With the Ultra68 camera used here, the ghost images appear to correlate with the quadrant of the intensifier upon which the images are formed and is strongest for the frame immediately following the laser pulse. This leads us to believe that the problem is associated with the phosphorescence lifetime of the phosphor screen in the intensifier. Although specific to the camera used here, this problem may also be encountered in other high-speed cameras, depending on their architecture. An effort is underway to quantify this artifact and remove it in the postprocessing of the images.

Another known issue is related to the spatial calibration procedure using the dot card. In the procedure discussed above, one assumption is that the laser sheet translates in a linear direction when, in fact, the laser sheet is actually rotating around a fixed point (i.e., the mirror). With the dot card mounted on a linear traversing mechanism, this introduces errors in determining the true spatial coordinates of each image, due to misalignment between the laser sheet and the dot card. For the small angles encountered here ($\sim$2 deg), this will have minimal effect on the calculated x-y position of each dot, but will cause an error in the assigned z coordinate for each image (where z is along the scan direction). In other words, the dot card is assumed to be at a constant z location, but the laser sheet is not. For the current work, this error is on the order of 1 mm (approximately 1 pixel) and is greatest at the edges of the image. As the distance from the scanning mirror to the test section decreases, however, this error will be larger. This may occur in flow facilities with limited physical or optical access. One solution would be to use a large lens, or f-theta lens, after the scanning mirror (with the mirror at the focal point of the lens) to form the laser sheets in parallel. This approach, however, is limited by the size and expense of the lens, which must have a diameter greater than the scan length.

The last item considered is that of the depth of field of the imaging system, as it is not possible to refocus a lens in real time. As such, the image may be out of focus at the front and back image planes if the appropriate lens settings are not chosen. A first-degree approximation of the depth of field (DOF) in an imaging system is given by

$$\mathrm{DOF} \cong 2f_{\mathrm{stop}} C \frac{M+1}{M^2} \qquad (3)$$

where f_{stop} is the f stop or speed of the lens (i.e., $f2.8$), C is the size of the circle of confusion (i.e., minimum resolvable spot size due to defocus), and M is the magnification. From this equation, it is clear that the DOF is proportional to the image resolution (C being the smallest feature). The DOF can be improved by reducing the aperture of the lens (increasing f_{stop}), but this will result in lower signal levels, due to a decreased solid angle for light collection. For the current experiment ($f_{\mathrm{stop}} = 2.8$, $M = 0.25$, and DOF $= 63.5$ mm), the minimum resolvable spot size is approximately 0.5 mm, which is approximately the same as the resolution of the images. Thus, this does not present a problem for these settings. For imaging of a subject closer to the camera or under low-level illumination, this issue may need to be considered in greater detail.

V.   Three-Dimensional Image Reconstruction

Figure 6 shows six images (out of 68 total slices) of a high-speed 3-D image sequence. Image 34 represents a plane through the center of the jet, and the remaining images represent planes offset from the jet center. As expected, the flow is dominated by the presence of axisymmetric ring vortices that are observed in all of the slices depicted in Fig. 6. In addition to these vortices, these images also display smaller-scale features for which the presence does not extend to all of the image planes shown here. These features, which are inherently 3-D, however, are difficult to observe and describe in the context of a 2-D image. As such, we use Tecplot, a commercial software package designed for use with computational fluid dynamics and numerical data, to display the 3-D image data in a suitable form for image analysis. Images are saved in an ASCII format file that records each image coordinate (x, y, z) and the associated intensity

Image 24	Image 29	Image 34
t = 48 μsec	t = 58 μsec	t = 68 μsec
Z = 22.4 mm	Z = 26.9 mm	Z = 31.8 mm

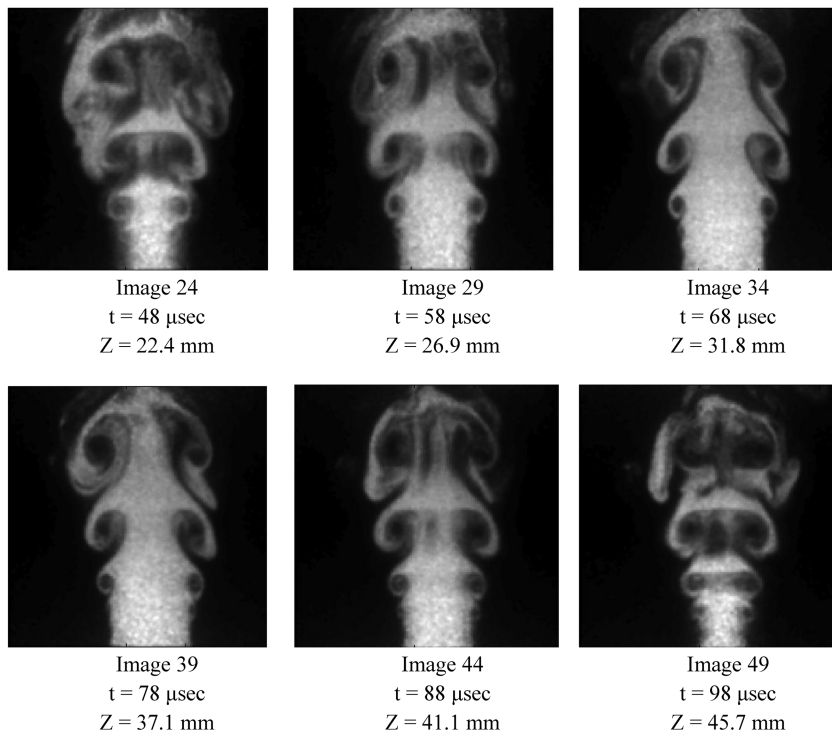| Image 39 | Image 44 | Image 49 |
| t = 78 μsec | t = 88 μsec | t = 98 μsec |
| Z = 37.1 mm | Z = 41.1 mm | Z = 45.7 mm |

Fig. 6   Images 24 through 49 of a 68-frame sequence, $Z = 0$ in corresponds to the start of the scan, scanning toward the camera.

value of the image. Tecplot is then able to render this data using isosurface and cross-sectional views, scaling the scanning axis to match the measurement volume.

Figure 7 displays an opaque isosurface fitted to an intensity value that corresponds to the edge of the seeded-flow region. In this fashion, a surface is fitted to the outer edge of the large-scale structures observed in Fig. 6. The resulting visualization presents a striking view of the 3-D structure contained in this nominally two-dimensional flow. The most noticeable feature of this image is the presence of long fingerlike structures that span the large vortex rings in the shear layer. These structures are distributed rather uniformly in the azimuthal direction and are observed in other images as well. The structures are elongated in the streamwise direction and are slightly cusped, possibly indicating the presence of counter-rotating streamwise vortex pairs.

These structures can also be observed in the 2-D images of Fig. 6, but without the detail shown in Fig. 7, making it quite difficult to visualize their presence in the flow or how they are connected to other features in the flowfield. With respect to the 3-D image quality, it is noteworthy that it is difficult to determine along which direction the laser sheet was scanned from the 3-D image. There are small sinusoidal type features that vary in the scan direction, however, that can be observed and are an artifact of the image reconstruction process. These are believed to be predominantly due to the gain/noise characteristics associated with the four-quadrant intensifier architecture of the camera, which amplifies the difference between images projected onto each quadrant.

Figure 8 is a rendering of the same image, but the outer surface is rendered transparent and a second surface is created to mark the inner structure of the flow. The transparent surface allows one to see how the outer surface of the jet rolls up with the vortex structure. The opaque inner surface corresponds to an intensity value slightly below that found at the jet centerline and effectively marks the point at which ambient fluid has mixed with the core fluid, thus lowering the local number density of seed particles and, therefore, the intensity observed in the image. This style of visualization complements the first image and allows one to explore the inner structure, where it can be observed that the azimuthally varying structure observed in Fig. 7 is not apparent on the opaque inner surface.

Although yielding extraordinary views of the flow, the isosurfaces present only a limited amount of the information contained in each 3-D image. To illustrate, Fig. 9 presents 12 cross-sectional slices (out of 220 possible) of the flow in an exploded view. These images are equivalent to what might be seen if the laser sheet was formed to
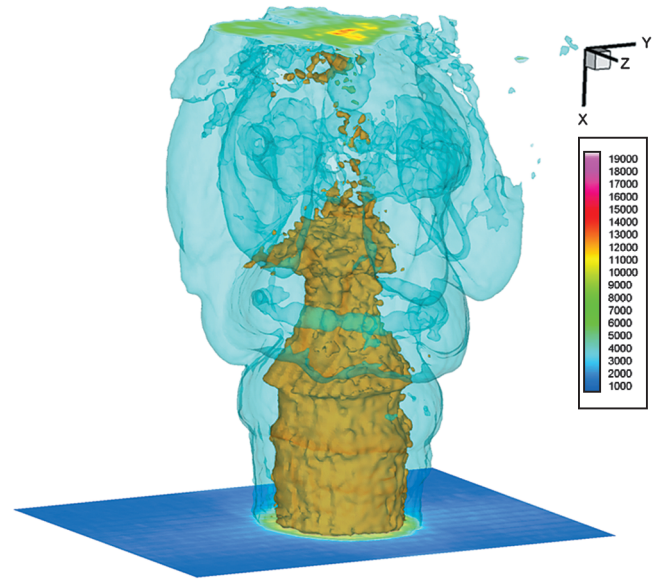

Fig. 8 Transparent isosurface visualization of the jet near field, $0.85x/D$ to $3.75x/D$.

illuminate a cross-stream plane and scanned in the streamwise direction (it was not). Again, it is difficult to tell what the actual scan direction was, indicating the ability of this 3-D flow visualization technique to acquire truly 3-D data about the flow structure. In this view, the near field of the jet is quite axisymmetric and dominated by ring vortices, with the transition to a more three-dimensional structure marked by azimuthal instabilities in the far field becoming quite clear.

Further analysis is possible through the formation of flow animations that can easily be rendered on a computer. Some possibilities
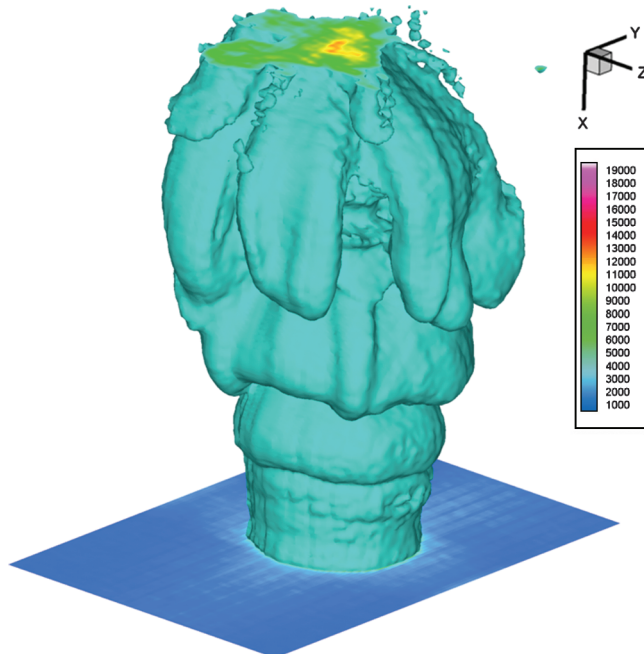

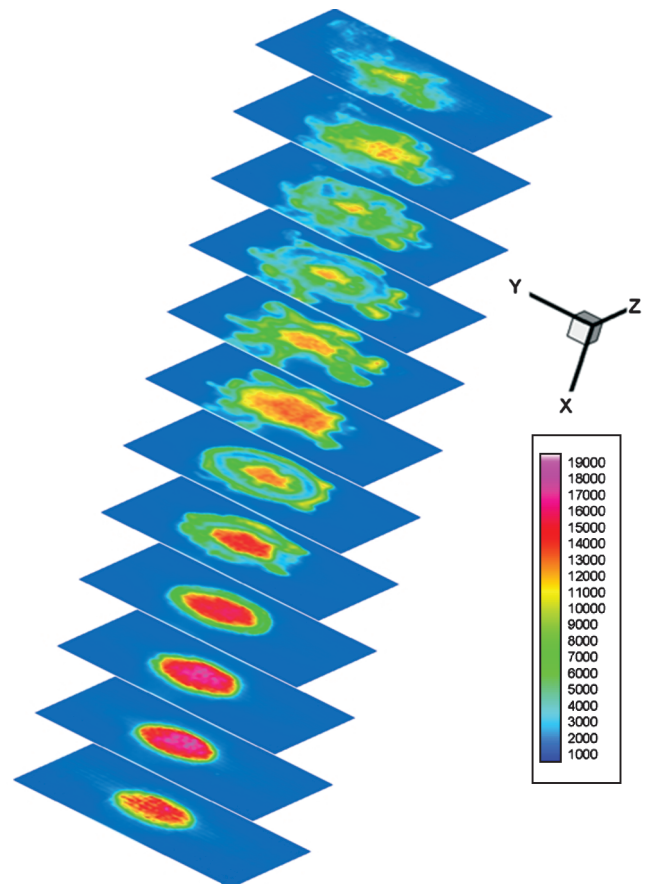**Fig. 7 Isosurface image of the near field, $0.85x/D$ to $3.75x/D$.**

Fig. 9 Z-Y slices of the jet near field, $0.85x/D$ to $3.75x/D$.

include rendering a large number of opaque surfaces at different intensity thresholds and stripping away each surface in a sequential fashion to peer further into the flow. Another particularly useful animation is to display a cross-sectional view that translates through the flowfield in a manner that is similar to the way the data were acquired. In addition, we have begun to use the proper orthogonal decomposition (POD) as a tool for data analysis, where POD is applied to 3-D flow visualization images to form a set of 3-D modes that best represent the features observed in the flow. More details on the application of 3-D POD can be found in Thurow and Lynch [28].

VI. Conclusions

A high-speed three-dimensional flow visualization system has been developed based on the scanning of a high-repetition-rate pulse-burst laser sheet through a flowfield using a galvanometric scanning mirror. A high-speed camera was used to record a sequence of 2-D images acquired at successive slices through the flowfield. The sequence of images was then reconstructed to form a 3-D visualization of the flow. The capabilities of this technique were demonstrated through the visualization of a round jet ($Re = 6700$) seeded with small water droplets. The nearly instantaneous 3-D images display striking features about the flow, including the presence of long fingerlike structures distributed around the periphery of the jet that would be very difficult to observe through conventional diagnostics. Although the 3-D flow physics (currently under investigation in a separate effort) was not the focus of this paper, these images clearly show the potential impact of this technique to explore the large-scale 3-D structure of a wide variety of unsteady 3-D flows. In essence, the technique outlined here can be applied to any flow or in any facility in which laser-sheet-based measurements (e.g., PLIF, etc.) are possible. This is due to the common characteristics of the instrumentation (Nd:YAG laser and CCD camera) used in these techniques. This is in contrast to techniques such as tomography and holography, which have additional constraints with respect to their experimental arrangement and are generally limited to particle-based flow measurements that may limit their application in some flows and facilities.

The main limiting factor (in terms of speed and resolution) of the technique outlined here is the technical specification of the high-speed camera employed in this work. In this work, images were acquired with $220 \times 220 \times 68$ voxel resolution over a time span of 136 μs. These specifications limit both the spatial and temporal resolution of the 3-D imaging technique. The pulse-burst laser and scanning mirror, on the other hand, are both capable of speeds an order of magnitude faster than that used here. It is worth noting that high-speed camera technology continues to develop at a rapid pace, with cameras under development that are potentially capable of 512×512 pixel resolution over 100 frames and rates in excess of 10 MHz. Thus, in the near future, the technique outlined here could produce higher-resolution images with a time resolution of 10 μs or less. Still, it should be emphasized that the present specifications are still quite impressive and suitable for a wide variety of fluid dynamics measurements.

In addition to refining the flow visualization aspects of this work, we will be expanding the general capability of the technique outlined here to obtain quantitative density measurements, such as those possible with LIF-based techniques. These techniques are well developed for 2-D measurements and use Nd:YAG lasers with characteristics similar to the pulse-burst laser described here. Thus, extension to a 3-D format should be relatively straightforward. To facilitate these efforts, the pulse-burst laser is currently undergoing a significant upgrade through the addition of two more amplification stages to increase its power output by nearly two orders of magnitude, and we expect to be able to produce pulses with energies in excess of 100 mJ/pulse. In addition, we are also in the process of adding a fourth-harmonic generator to allow for frequency conversion to 266 nm (ultraviolet), in support of acetone-vapor fluorescence. These new additions will substantially increase the quality of images and allow the system to be used for imaging other flowfields.

References

[1] Wu, P., Lempert, W., and Miles, R., "Megahertz Pulse-Burst Laser and Visualization of Shock-Wave/Boundary-Layer Interaction," *AIAA Journal*, Vol. 38, No. 4, 2000, pp. 672–679.
doi:10.2514/2.1009

[2] Wu, P., and Miles, R., "Megahertz Visualization of Compression-Corner Shock Structures," *AIAA Journal*, Vol. 39, No. 8, 2001, pp. 1542–1546.
doi:10.2514/2.1478

[3] Thurow, B., Samimy, M., and Lempert, W., "Structure of a Supersonic Impinging Rectangular Jet via Real-Time Optical Diagnostics," AIAA Paper 2002-2865, June 2002.

[4] Samimy, M., and Wernet, M. P., "Review of Planar Multiple-Component Velocimetry in High-Speed Flows," *AIAA Journal*, Vol. 38, No. 4, 2000, pp. 553–574.
doi:10.2514/2.1004

[5] Wernet, M., "Time Resolved PIV for Space-Time Correlations in Hot Jets," AIAA Paper 2007-47, Jan. 2007.

[6] Thurow, B., Jiang, N., Lempert, W., and Samimy, M., "Development of Megahertz-Rate Planar Doppler Velocimetry for High-Speed Flows," *AIAA Journal*, Vol. 43, No. 3, 2005, pp. 500–511.
doi:10.2514/1.7749

[7] Kaminski, C. F., Hult, J., and Ald'en, M., "High Repetition Rate Planar Laser Induced Fluorescence of OH in a Turbulent Non-Premixed Flame," *Applied Physics B*, Vol. 68, No. 4, 1999, pp. 757–760.
doi:10.1007/s003400050700

[8] Dreizlerl, A., Lindenmaier, S., Maas, U., Hult, J., Ald'en, M., and Kaminski, C. F., "Characterisation of a Spark Ignition System by Planar Laser-Induced Fluorescence of OH at High Repetition Rates and Comparison with Chemical Kinetic Calculations," *Applied Physics B*, Vol. 70, No. 2, 2000, pp. 287–294.
doi:10.1007/s003400050047

[9] Guezennec, Y. G., Brodkey, R. S., Trigui, J., and Kent, J. C., "Algorithms for Fully Automated Three-Dimensional Particle Tracking Velocimetry," *Experiments in Fluids*, Vol. 17, 1994, pp. 209–219.
doi:10.1007/BF00203039

[10] Trolinger, J. D., Rottenkolber, M., and Elandaloussi, F., *Measurement Science and Technology*, Vol. 8, No. 12, 1997, pp. 1573–1583.
doi:10.1088/0957-0233/8/12/020

[11] Sheng, J., Malkiel, E., and Katz, J., "Single Beam Two-Views Holographic Particle Image Velocimetry," *Applied Optics*, Vol. 42, No. 2, 2003, pp. 235–250.
doi:10.1364/AO.42.000235

[12] Elkins, C. J., Markl, M., Pelc, N., and Eaton, J. K., "4D Magnetic Resonance Velocimetry for Mean Velocity Measurements in Complex Turbulent Flows," *Experiments in Fluids*, Vol. 34, 2003, pp. 494–503.
doi:10.1007/s00348-003-0587-z

[13] Kychakoff, G., Paul, P. H., Van Cruyningen, I., and Hanson, R. K., "Movies and 3-D Images of Flowfields Using Planar Laser Induced Fluorescence," *Applied Optics*, Vol. 26, No. 13, 1987, pp. 2498–2500.
doi:10.1364/AO.26.002498

[14] Long, M. B., and Yip, B., "Measurement of Three-Dimensional Concentrations in Turbulent Jets and Flames," *Proceedings of the 21st Symposium on Combustion*, Combustion Inst., Pittsburgh, PA, 1988, pp. 701–709.

[15] Yip, B., Schmitt, R. L., and Long, M. B., "Instantaneous, Three-Dimensional Concentration Measurements in Turbulent Jets and Flames," *Optics Letters*, Vol. 13, No. 2, 1988, pp. 96–98.
doi:10.1364/OL.13.000096

[16] Patrie, B. J., Seitzman, J. M., and Hanson, R. K., "Instantaneous Three-Dimensional Flow Visualization by Rapid Acquisition of Multiple Planar Flow Images," *Optical Engineering*, Vol. 33, No. 3, 1994, pp. 975–980.
doi:10.1117/12.160888

[17] Goldstein, J. E., and Smits, A. J., "Flow Visualization of the Three-Dimensional, Time-Evolving Structure of a Turbulent Boundary Layer," *Physics of Fluids*, Vol. 6, 1994, pp. 577–587.

doi:10.1063/1.868353

[18] Island, T. C., Patrie, B. J., Mungal, M. G., and Hanson, R. K., "Instantaneous Three-Dimensional Flow Visualization of a Supersonic Mixing Layer," *Experiments in Fluids*, Vol. 20, 1996, pp. 249–256.
doi:10.1007/BF00192669

[19] Brucker, C. H., "3D Scanning PIV Applied to an Air Flow in a Motored Engine Using Digital High-Speed Video," *Measurement Science and Technology*, Vol. 8, No. 12, 1997, pp. 1480–1492.
doi:10.1088/0957-0233/8/12/011

[20] Delo, C., and Smits, A. J., "Volumetric Visualization of Coherent Structure in a Low Reynolds Number Turbulent Boundary Layer," *International Journal of Fluid Dynamics*, Vol. 1, 1997, Paper 3.

[21] Hult, J., Omrane, A., Nygren, J., Kaminski, C. F., Axelsson, B., Collin, R., Bengtsson, P.-E., and Alden, M., "Quantitative Three-Dimensional Imaging of Soot Volume Fraction in Turbulent Non-Premixed Flames," *Experiments in Fluids*, Vol. 33, 2002, pp. 265–69.
doi:10.1007/s00348-002-0410-2

[22] Tian, X., and Roberts, P. J. W., "A 3D LIF System For Turbulent Buoyant Jet Flows," *Experiments in Fluids*, Vol. 35, 2003, pp. 636–647.
doi:10.1007/s00348-003-0714-x

[23] Lempert, W. R., Wu, P., Zhang, B., Miles, R. B., Lowrance, J. L., Mastracola, V., and Kosonocky, W. F., "Pulseburst Laser System for High Speed Flow Diagnostics," AIAA Paper 96-0179, Jan. 1996.

[24] Thurow, B., Hileman, J., Samimy, M., and Lempert, W., "A MHz Rate Imaging System for Study of Turbulent and Time Evolving High Speed Flows," *Proceedings of the 19th International Congress on Instrumentation in Aerospace Simulation Facilities*, Inst. of Electrical and Electronics Engineers, Piscataway, NJ, Aug. 2001, pp. 37–47.
doi:10.1109/ICIASF.2001.960234

[25] Thurow, B., Satija, A., and Lynch, K., "Third-Generation MHz Rate Pulse Burst Laser System," *Applied Optics*, Vol. 48, No. 11, 2009, pp. 2086–2093.
doi:10.1364/AO.48.002086

[26] Koechner, W., *Solid State Laser Engineering*, 6th ed., Springer Science and Business Media, New York, 2006.

[27] Thurow, B., and Satija, A., "Preliminary Development of a Nearly-Instantaneous Three-Dimensional Imaging Technique for High-Speed Flow Fields," AIAA Paper 2006-2972, June 2006.

[28] Thurow, B., and Lynch, K., "3-D POD Analysis of a Naturally Excited Jet," AIAA Paper 2008-4067, June 2008.

R. Lucht
Associate Editor